



UvA-DARE (Digital Academic Repository)

Modelling flow-induced vibrations of gates in hydraulic structures

Erdbrink, C.D.

Publication date
2014

[Link to publication](#)

Citation for published version (APA):

Erdbrink, C. D. (2014). *Modelling flow-induced vibrations of gates in hydraulic structures*. [Thesis, fully internal, Universiteit van Amsterdam].

General rights

It is not permitted to download or to forward/distribute the text or part of it without the consent of the author(s) and/or copyright holder(s), other than for strictly personal, individual use, unless the work is under an open content license (like Creative Commons).

Disclaimer/Complaints regulations

If you believe that digital publication of certain material infringes any of your rights or (privacy) interests, please let the Library know, stating your reasons. In case of a legitimate complaint, the Library will make the material inaccessible and/or remove it from the website. Please Ask the Library: <https://uba.uva.nl/en/contact>, or a letter to: Library of the University of Amsterdam, Secretariat, Singel 425, 1012 WP Amsterdam, The Netherlands. You will be contacted as soon as possible.

6 Numerical simulation study of gate vibration⁵

6.1 Introduction

Physics-based numerical simulations of gate vibrations that give the displacement of the gate in time are inevitably complex and computationally involved. The computational Fluid-Structure Interaction (FSI) model needs to deal with very small displacements of varying frequencies and should represent the boundary forces accurately (see Chapter 3). Many modelling simplifications, such as lowering the fluid's viscosity or including only partial interaction between fluid and solid, are not permitted as they misrepresent the physics too drastically so that excitation mechanisms have no chance to develop correctly. Meshes that do not match up at the fluid-solid interface have the disadvantage of requiring interpolation functions (De Boer 2008) and dedicated load transfer schemes (Jaiman et al., 2006). Rugonyi and Bathe (2001) explore FEM for FSI problems with incompressible fluid flow.

It was clarified in previous chapters that studies flow-induced vibrations of bluff bodies in general usually relate to vortex-induced vibrations (VIV) which differs fundamentally from gate vibrations. Examples for the famous problem of flow around stationary and vibrating cylinders are Al-Jamal and Dalton (2004) and Dai et al. (2013). Numerical modelling of gates often has the goal of verifying the design of a specific hydraulic structure. Determining static support forces is then a greater concern than addressing vibrations (Scheffermann and Stockstill, 2009; Liu et al., 2011). Those studies that do consider vibrations more often than not fail to make links to the existing state of the art, thus not optimally contributing to fundamental knowledge (e.g. Lupuleac et al. 2007).

6.2 Model set-up

The goal of the numerical simulations is to describe the physical features that are decisive for causing the difference in response between the two gate types that were introduced in the previous chapter; a standard rectangular gate and a rectangular gate with ventilation slots added. The numerical model is two-dimensional in the vertical direction (2DV), see the figure in Section 5.2. Model dimensions are identical to the physical scale model. The flow-wise model length is 3.5 m. The static vertical equilibrium is achieved by a suspension support force equal to the difference between gravitational and buoyancy and mean lift forces. The flow velocity vector is defined as $\mathbf{u} = (u, v)$. The fluid flow is modelled by the incompressible Reynolds-Averaged Navier-Stokes (RANS) equations in combination with the standard k - ϵ turbulence model. The governing equations are:

$$\rho \frac{\partial \bar{\mathbf{u}}}{\partial t} + \rho \bar{\mathbf{u}} \cdot \nabla \bar{\mathbf{u}} + \nabla \cdot \overline{(\rho \mathbf{u}' \otimes \mathbf{u}')} = -\nabla \bar{p} + \nabla \cdot \mu (\nabla \bar{\mathbf{u}} + (\nabla \bar{\mathbf{u}})^T) + \mathbf{F}_g,$$

⁵ This chapter is based on and uses text and content from “Reducing cross-flow vibrations of underflow gates: experiments and numerical studies” by C.D. Erdbrink, V.V. Krzhizhanovskaya, P.M.A. Sloot, currently under review at the Journal of Fluids and Structures.

$$\text{and } \nabla \cdot \bar{\mathbf{u}} = 0, \quad (6.1)$$

where ρ is density of water, μ is the dynamic viscosity of water, p is the water pressure, bars indicate time-averaged values and primes indicate variational variables, according to the Reynolds decomposition. The gravity term is a force per unit volume:

$$\mathbf{F}_g = \begin{pmatrix} 0 \\ -\rho g \end{pmatrix}. \quad (6.2)$$

The k - ε turbulence model provides closure by solving a coupled pair of PDE's for turbulent kinetic energy k and turbulent dissipation ε (see section 3.3 and COMSOL 2013). For the boundary conditions of the fluid domain, there is a block velocity at the inlet:

$$\mathbf{u} = \begin{pmatrix} U_0 \\ 0 \end{pmatrix}, \quad (6.3)$$

with U_0 a chosen constant. At the outlet a hydrostatic pressure profile is imposed: $p(y) = (h_{out} - y)\rho g$, where h_{out} is the water depth at the outlet, equal to the height of the flow domain. The bottom flow boundary is $\mathbf{u} = 0$, no slip with a wall function describing the near-wall velocity profile. The boundary at the water surface is $\mathbf{u} \cdot \mathbf{n} = 0$, free slip or 'rigid lid', with \mathbf{n} the normal vector.

For the initial conditions of the fluid domain, we have at $t = 0$, $p = 0$ for all (x, y) , and $\mathbf{u} = (U_0 S(t) \ 0)^T$, with $S(t)$ a smooth S-curve increasing from 0 to 1 for $0 < t < 0.5$ s. The wall function condition for full resolution consists of wall lift-off (dimensionless wall distance) of $y^+ = 11.06$ with:

$$y^+ = \frac{\rho u_\tau y}{\mu} \text{ with shear or friction velocity } u_\tau = C_\mu^{1/4} \sqrt{k}. \quad (6.4)$$

This prescribes the distance at which the viscous sub-layer and the logarithmic layer meet (see e.g. COMSOL, 2013).

The description of the solid domain includes displacement of the whole body, with displacement vector \mathbf{u}_s , and deformation due to stresses. Defining $\mathbf{u}_s = (u_{s,x}; u_{s,y})$ and $\boldsymbol{\sigma}_s$ as the stresses it experiences, we have

$$\rho_s \frac{\partial^2 \mathbf{u}_s}{\partial t^2} - \nabla \cdot \boldsymbol{\sigma}_s = \mathbf{F}_v. \quad (6.5)$$

The applied external forces \mathbf{F}_v acting on the gate body are

$$\begin{aligned} \mathbf{F}_v &= \mathbf{F}_g + \mathbf{F}_{\text{spring}} + \mathbf{F}_{\text{damp}} + \mathbf{F}_{\text{water}} + \mathbf{F}_{\text{suspension}} = \\ & \begin{pmatrix} 0 \\ -\rho_s g \end{pmatrix} + \begin{pmatrix} 0 \\ -k u_{s,y} - c \dot{u}_{s,y} \end{pmatrix} + \mathbf{F}_{\text{water}} + \mathbf{F}_{\text{suspension}}, \end{aligned} \quad (6.6)$$

where $\mathbf{F}_{\text{water}}$ represents the dynamic load of the water flow on the submerged part of the solid. The spring and damping forces depends on chosen constants for stiffness (k) and damping (c). The last force represents the steady suspension force in the structural element that connects the gate object with the bigger (fixed) structure. The constitutive relation, or stress-strain relation, can be written as $\boldsymbol{\sigma}_s = \boldsymbol{\sigma}_0 + \mathcal{C} : (\boldsymbol{\varepsilon} - \boldsymbol{\varepsilon}_0)$ with sub-indices 0 indicating initial values, \mathcal{C} the elasticity tensor representing material properties (Young's modulus and Poisson ratio) and $:$ denoting the double-dot tensor product. The strain tensor is given by $\boldsymbol{\varepsilon}_s = 1/2 (\nabla \mathbf{u}_s + \nabla \mathbf{u}_s^T)$, which is equivalent to

$$\varepsilon_{xx} = \frac{\partial u}{\partial x}, \varepsilon_{yy} = \frac{\partial v}{\partial y} \text{ and } \varepsilon_{xy} = \varepsilon_{yx} = \frac{1}{2} \left(\frac{\partial u}{\partial y} + \frac{\partial v}{\partial x} \right). \quad (6.7)$$

The displacement of the solid is fixed in horizontal direction: $u_{s,x} = 0$ and the initial conditions of the solid domain are $\mathbf{u}_s = 0$ and $\partial \mathbf{u}_s / \partial t = 0$. The load that the water flow forces exert on the boundaries of the solid body, $\mathbf{F}_{\text{water}}$, is defined as a force per unit area $\mathbf{F}_{\text{water}} = \mathbf{T} \cdot \mathbf{n}$ (in N/m²), where \mathbf{n} is the normal vector on the solid boundary and \mathbf{T} is the 2x2 tensor containing all stresses of the flow. The normal stresses, on the diagonal of \mathbf{T} , represent the pressure. The remaining elements of \mathbf{T} represent the viscous shear stresses – each of these elements consist of a stress contribution from the turbulent viscosity (μ_T) and from the laminar viscosity (μ). At $t = 0$, $\mathbf{F}_{\text{water}} = 0$. For $0 < t \leq 0.5$ s the force on the boundary increases according to the same sigmoid function $S(t)$ as for the flow velocity: $\mathbf{F}_{\text{water}} = \mathbf{T} \cdot \mathbf{n} \cdot S(t)$.

The ALE method is again used to make a moving mesh for the entire model domain, see also Section 3.3. This means that the mesh covers fluid and solid domain together. The mesh adapts to the translational motion of the gate without changing its connectivity. The initially straight upper fluid boundary, the rigid lid, slightly bends up and down along with the gate, as it is part of the ALE mesh. The boundary conditions for the mesh displacement vector \mathbf{u}_m are

$$\begin{aligned} u_{m,x} &= 0 \text{ on the fluid surface boundaries,} \\ \mathbf{u}_m &= 0 \text{ on all remaining boundaries of the fluid domain,} \\ \mathbf{u}_m &= \mathbf{u}_s \text{ on the solid boundaries.} \end{aligned} \quad (6.8)$$

For the inner area, the mesh deformation is smoothed using 'hyper-elastic smoothing', inspired by an description of neo-Hookean materials, an approach that seeks for a minimum of 'mesh deformation energy' (see COMSOL 2013). This smoothing type proved more robust during the preliminary runs than the Winslow type used in Chapter 4.

Again the finite element method (FEM) is used. The model is called "model II" in Table 1 in Section 3.3.3. The transient runs are preceded by steady-state pre-runs with the gate held fixed in order to iteratively determine the inlet velocity at which the upstream pressure away from the gate is zero at the surface. The grid consists of unstructured triangular elements and inflated boundary refinements adjacent to the gate walls and flow bottom. A typical grid contained around 35,000 elements and 200,000 degrees of freedom. The cell size

in the near-wall flow regions is dictated by the dimensionless wall distance by ensuring that $y^*_{\max} = 11.06$ at all walls where wall functions are applied; this was checked after each run.

The FEM solver COMSOL Multiphysics v4.3a (COMSOL 2013) is used to solve the system of equations of seven dependent variables. The solution procedure is solved in a fully coupled way with the PARDISO direct solver. The implicit backward differentiation formula (BDF) with adaptive time stepping is used, an extension of the backward Euler method for variable order. The simulations were done on a cluster, using 24 cores on a single node. Typically, three seconds of simulated time took around 12 hours of computing time.

6.3 Selected cases and model validation

Two cases from the experimental data set are selected for simulation; these are representative of strong vibrations in the low and high V_r region. See Table 6.1.

Table 6.1. Selected cases for numerical simulations (values from experiment).

	Q (l/s)	k (N/m)	h_l (m)	Δh (m)	a/D (-)	V_r (-)	C_s (-)	f_z (Hz)	\bar{F}_z (N)
case 1	23	82502	0.398	0.088	1.00	2.6	5.2	10.1	25.6
case 2	40	19298	0.605	0.285	0.86	10.2	5.5	4.66	63.0

We are interested in the behaviour of both gates for conditions as close as possible to those found in the experiment. The followed approach was to assign applicable physical parameters from the experiment to the numerical model. Firstly, the added mass coefficient m_w in still water is derived from a zero discharge model and compared to experimental values. Secondly, iterative validation runs are made in a model *with* discharge to achieve the settings necessary for attaining the response frequency as found in the experiment. These two preparatory modelling steps should be seen as efforts towards model validation (comparing the modelled value of a universal physical parameter with the experimental value) and calibration (adjusting the numerical model for the specific modelling task), respectively.

6.3.1 Added mass validation

The kinetic energy approach is followed to find m_w in still water. Because flow velocities are low, the laminar incompressible flow equations are solved. The oscillating gate is simulated by a moving wall with a prescribed vertical periodic velocity with a frequency of 4.7 Hz and amplitude of 0.15 m/s. The rigid lid assumption is justified for this situation because the wave radiation effect is small: for $h = 0.40\text{m}$, we have $\omega^2 h/g = 36 \gg 10$, the usual criterion for wave radiation (Kolkman, 1976).

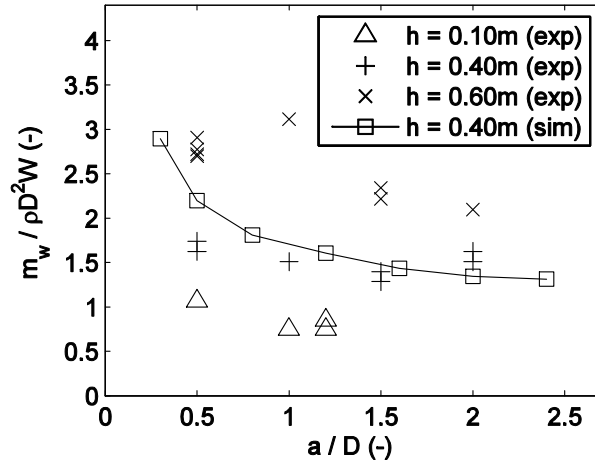


Figure 6.1. Added mass coefficient in still water for various openings a and water depths h , from experiment (exp) and simulations (sim).

In Figure 6.1 experimental values of non-dimensional added mass in still water are plotted for three water depths, together with simulation results for $h = 0.40$ m. The added mass simulations show that the wall proximity effect at low a/D is somewhat more pronounced than in the available experimental values. For vibrations at high gate openings, the influence of the bottom disappears. The simulations show a gradient reduction in correspondence with this, while experimental data at higher a/D would be needed to cover this stabilisation. Experimental data by Nguyen (1982) in Naudascher and Rockwell (1994) show stabilisation of the added mass for $a/D > 2-3$. The dependence on water depth that is shown by the experimental values is not sufficiently captured by the FEM model: for other water depths, the results are too close to the plotted relation for $h = 0.40$ m. The influence of domain width was neutralised by ignoring very small flow velocities in the computation, at distances far away from the gate. In summary, for the combinations of water depths and gate openings that are considered in this study, the physical added mass is reasonably well approximated by the numerical model.

6.3.2 Artificial added coefficients

In the numerical model, the gate mass is defined by assigning a solid density ρ_s , and the suspension stiffness k is defined in a spring suspension support. The added rigidity k_w due to buoyancy is in all studied cases negligibly small, i.e. $k_w \ll k$. Despite the fact that for oscillating bodies in flowing water m_w and k_w are in general not equal to their still water values (nor constants for that matter), it is reasoned that mismatches of simulated response frequencies with experimental values, must be traced back to artificial added coefficients. Such misrepresentations were indeed found. It was checked that the natural frequency of the isolated gate in vacuum calculated by the same FEM model exactly matched the analytical value.

A possible cause of numerical complications in FSI is the so-called 'artificial added mass' effect. This has been investigated and partially described and explained for sequentially

staggered schemes (Förster et al., 2007), but no literature was found for FSI with fully coupled schemes in FEM for relatively stiff solids. Similar to Jamal and Dalton (2004), we define the mass factor m^* to be the ratio of solid density over fluid density. The term “mass ratio” is also used for this sometimes but can be confused with the dimensionless mass m_r . The sensitivity of the simulated response frequency $f_{z,num}$ to the mass factor m^* is plotted in Figure 6.2.

Using the true mass factor of the experiment, which is less than one, gives crude underestimates of the measured response frequency $f_{z,exp}$ for both investigated cases. The mass factor is increased to $m^* = 1.1$ simply by using a lower gate height in the simulation than in the experiment. When m^* is increased further by means of increasing solid density ρ_s , while at the same time adjusting k proportionally such that the dry natural frequency f_0 remained constant, the numerical model gives better estimates of $f_{z,exp}$. Grid refinements did not noticeably influence the trends.

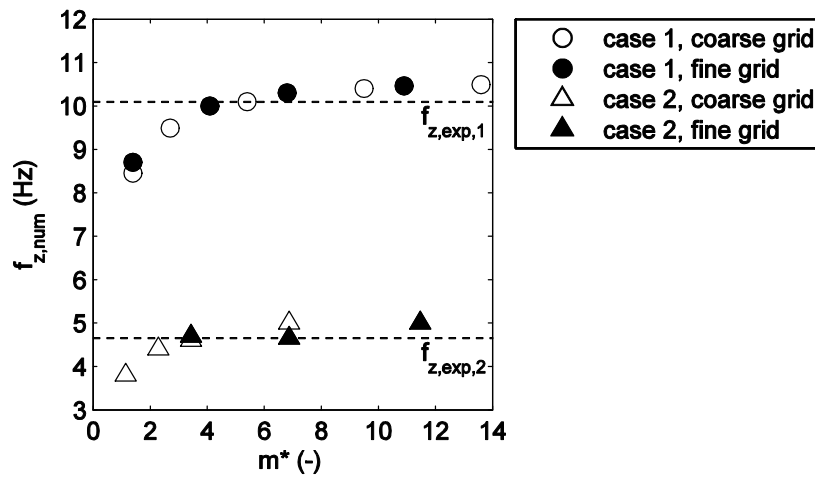


Figure 6.2. The artificial added mass effect for the two cases of Table 1. The simulated frequencies $f_{z,num}$ are given for different mass factors m^* . For both cases, all data points have the same theoretical natural frequency. The horizontal lines show the experimental response frequencies $f_{z,exp}$.

Increasing m^* at fixed f_0 does not yield an asymptotic approach to the experimental values, however. In addition, the achieved displacement amplitudes of the gate vibration are inconveniently small for $m^* \geq 10$ (order 0.1 mm and smaller). As a tradeoff it is decided to take $m^* = 3$ and adapt k accordingly so that natural frequency and response frequency are well represented by the numerical model for both cases and displacements are in order of millimeters. It is noted that this measure distorts the absolute values of the modelled displacements.

6.4 Results of calibrated numerical model

Next, cases 1 and 2 were simulated with the calibrated numerical model. In each transient run, only three to four seconds were simulated. The numerical perturbations related to initialisation of the run were enough to kick-start a vibration – then the simulated vibration

either quickly grew in amplitude or damped out. After a substantial number of test runs, no active response has been found for case 1 for neither gate type. This is presumably related to an underestimation of the dynamics of the impinging shear layer, see Section 4.1. For case 2 growing amplitudes were found at a slightly larger gate opening than in the experiment (46 mm in the simulation versus 43 mm in the experiment). All plots in this section are simulations of case 2; subsequent analysis also focuses on case 2. Movies of simulation case 2 in the online material show pressure, velocity and turbulent kinetic energy fields for both gates.

Figure 6.3 shows time signals of the simulated displacement normalized to the gate width D . After an initially similar disturbance, the ventilated gate follows a damped vibration and the original gate is amplified. The frequency of the ventilated gate is a little lower than the closed gate.

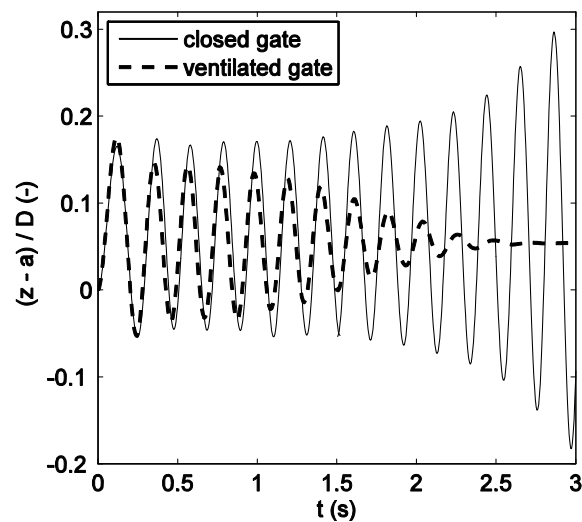


Figure 6.3. Simulated vertical displacements of original, closed gate (thin continuous line) and gate with ventilation slots added (thick dashed line). The displacement is plotted relative to the original gate position $z = a$ and normalized to the gate width D .

Zooming in on the gate response, Figure 6.4 provides a closer look on the displacement signal, giving also acceleration and lift force oscillation.

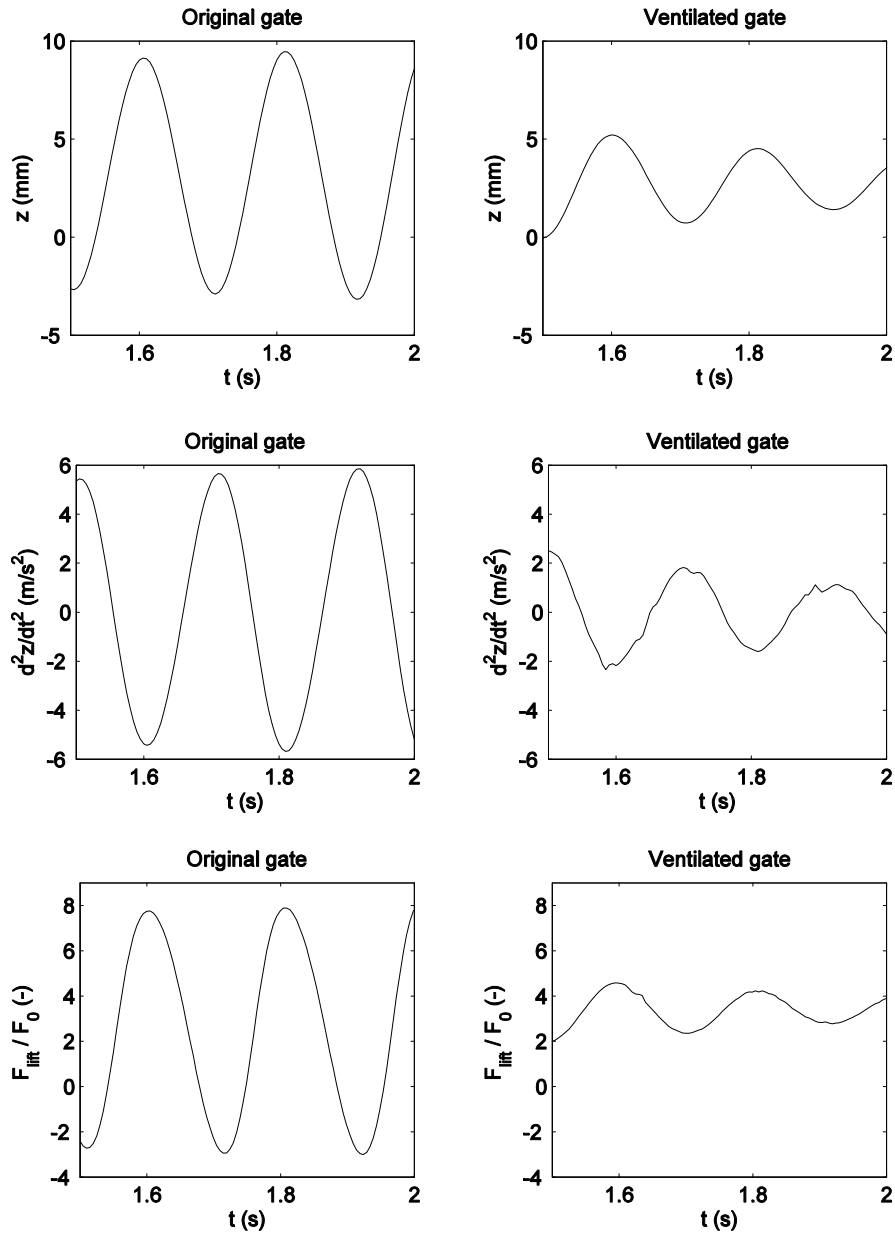


Figure 6.4. Simulation case 2: time signal excerpts of gate displacement, gate acceleration and dimensionless lift force, for both gate types. The acceleration is computed with a first-order finite-difference scheme without filtering.

For further comparison of the modelled response of both gate types, a number of profile plots is made in Figures 6.6-6.10. Figure 6.5 gives the locations of output profiles for pressure, velocity and turbulent kinetic energy, which are plotted in Figures 6.6-6.10.

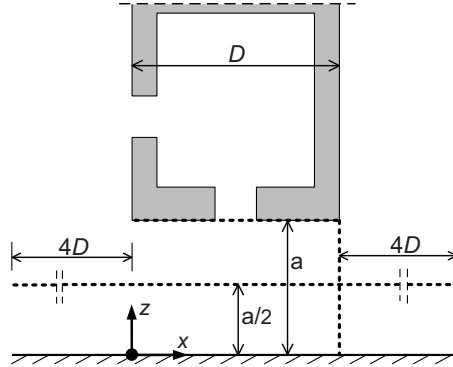


Figure 6.5. Location of output profiles (dashed lines) used in Figures 6.6-6.10.

In each plot of Figures 6.6-6.10, the nine thin lines correspond to different moments in one full sine period, according to $i\pi/4$ with $0 \leq i \leq 8$, starting in equilibrium position (moving upwards) at $t = 1.35$ s. For the original gate, the i values are indicated explicitly. Additionally, Figures 6-10 display the situation where the gate is fixed at the equilibrium position for both gate types. The variation of flow parameters is much smaller in the fixed gate scenario and therefore these are depicted as single thick dashed lines, which denote time-averaged values over two consecutive periods, after four seconds of simulation. Figures 6.6-6.10 show that the oscillating ventilated gate experiences significantly lower periodic variation in streamwise pressure, velocity and turbulent kinetic energy (TKE) at the trailing edge, and in bottom pressure, than the gate without holes. Obviously this is associated with the difference in displacement amplitude at the time of output, but nevertheless an insightful comparison can be made.

The streamwise pressure plot (Figure 6.6) shows that, at a height of half the gate opening, the original gate experiences larger temporal variation and higher maximum streamwise pressure gradients directly under the gate ($0 < x/D < 1$) than the ventilated gate. The latter experiences low $|dp/dx|$ -values for $x/D < 2$. The u -velocity profiles (Figure 6.7) clearly show the influence of the extra stream through the hole. For the ventilated gate the area of negative streamwise velocity is very limited, $0.8 < z/a < 1$ versus $0.7 < z/a < 1$ for the original gate, and the negative u -velocities are much smaller as well.

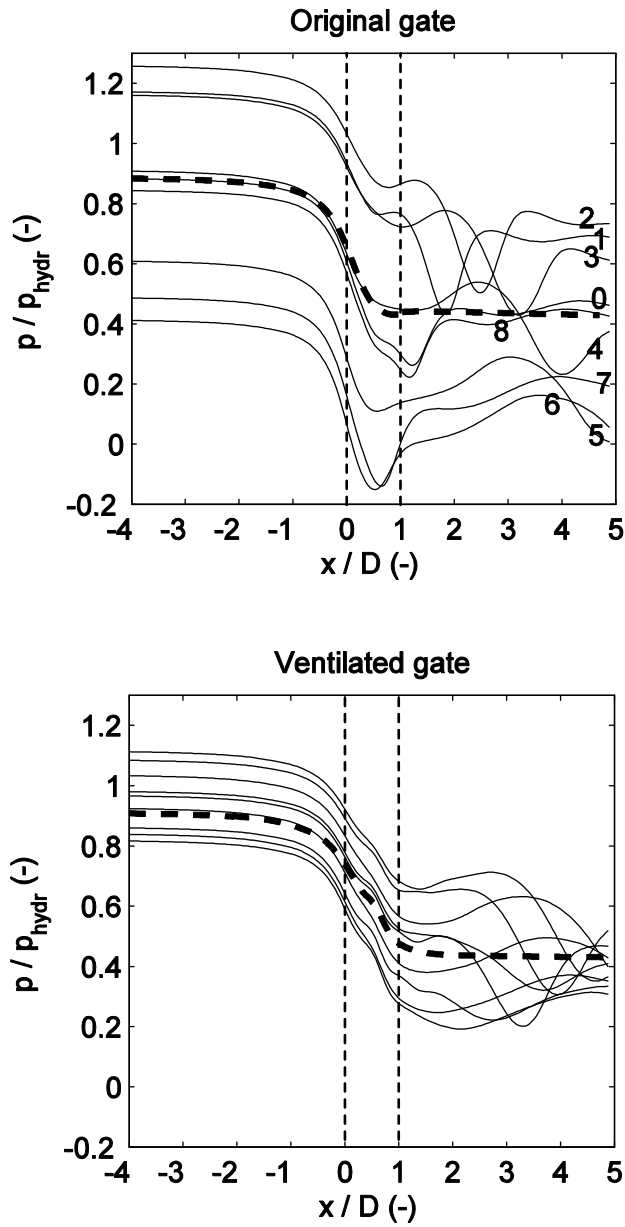


Figure 6.6. Simulated streamwise pressure variation at $z = a/2$ for moving gate without (left) and with ventilation holes (right); p_{hydr} is the hydrostatic pressure at $z = a/2$. Thick dashed lines show the situation where the gate is held fixed. Vertical thin dashed lines indicate location of the gate. The nine lines correspond to different moments in one full period, according to $i\pi/4$ with $0 \leq i \leq 8$.

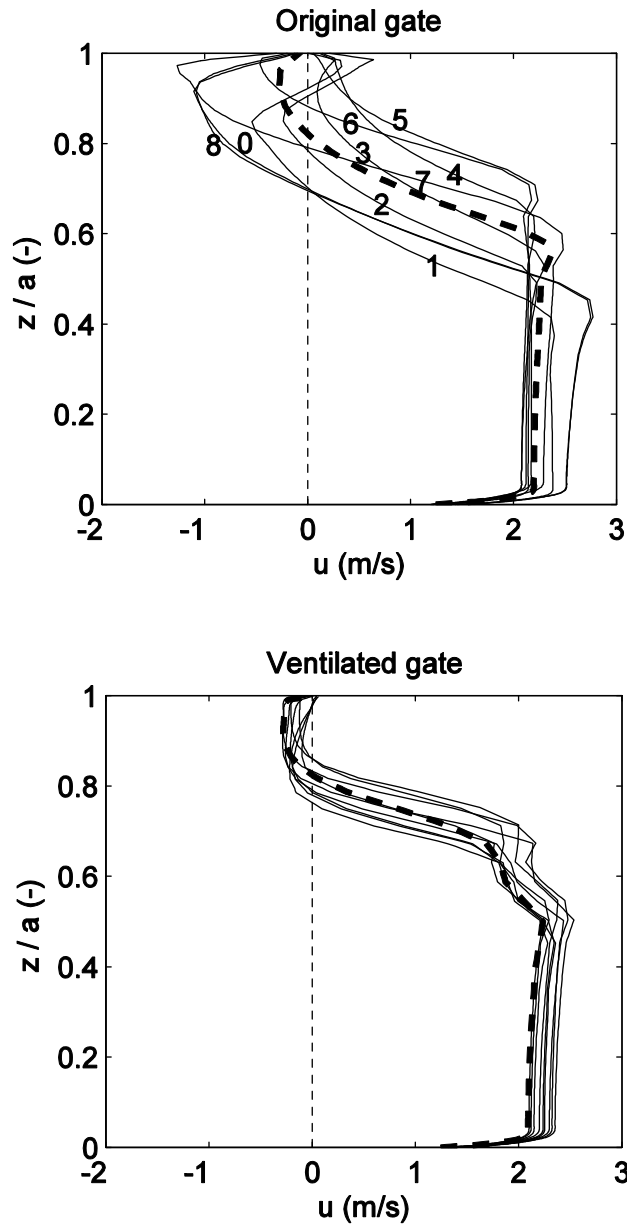


Figure 6.7. Simulated vertical profile of horizontal velocity component u at downstream gate edge. (from bottom to gate). Thick dashed lines indicate the fixed gate scenario. Positive values indicate the mean streamwise direction.

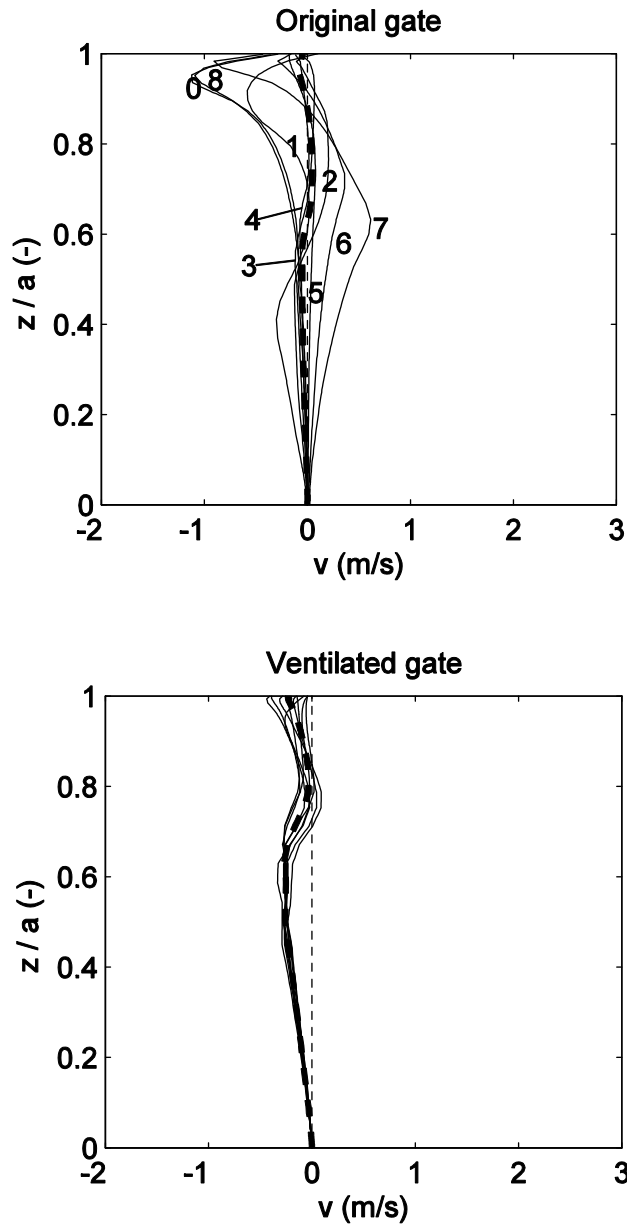


Figure 6.8. Simulated vertical profile of vertical velocity component v at downstream gate edge. (from bottom to gate). Thick dashed lines indicate fixed gate scenario. Positive values indicate upward direction.

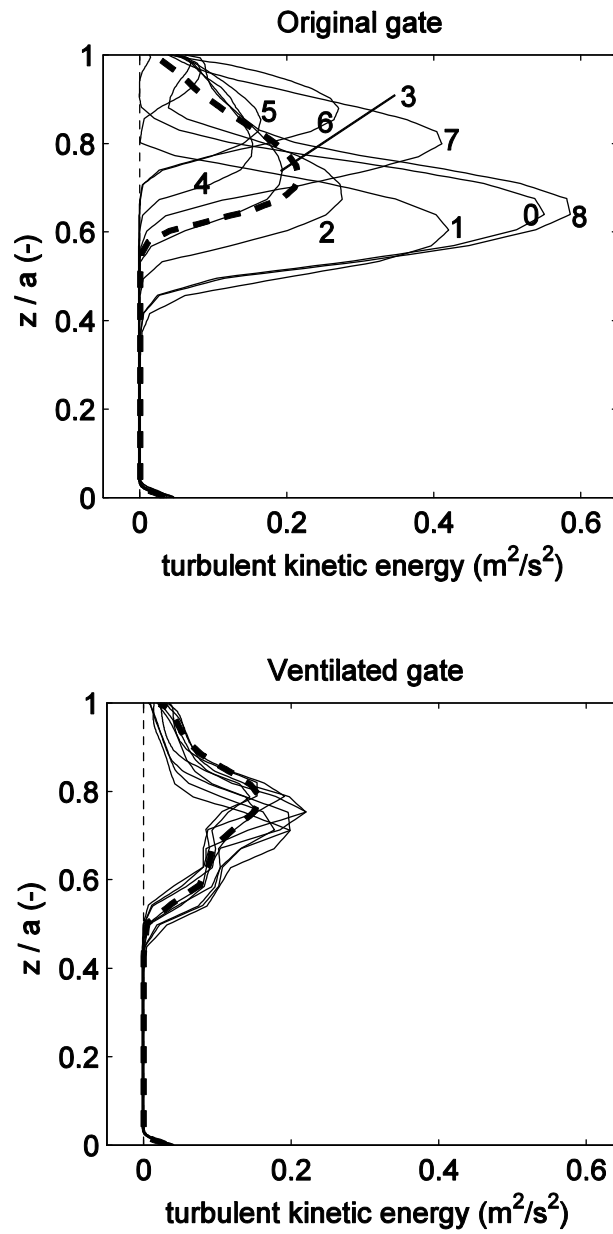


Figure 6.9. Turbulent kinetic energy in vertical profile at the trailing edge of the gate. Thick dashed lines indicate fixed gate scenario.

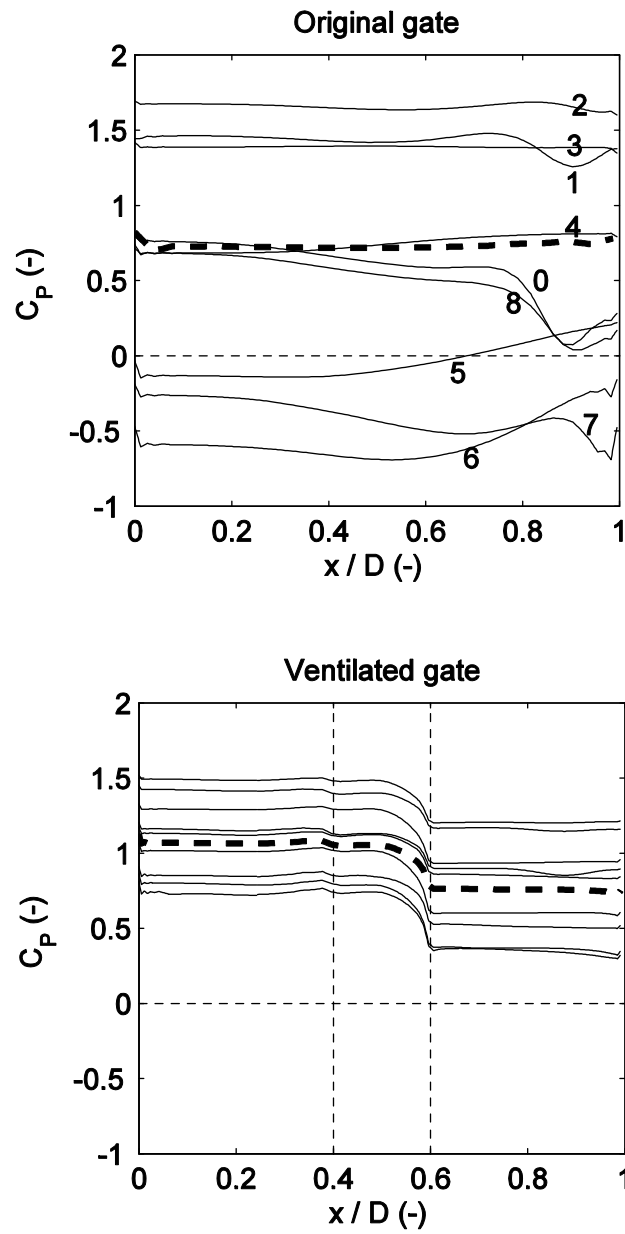
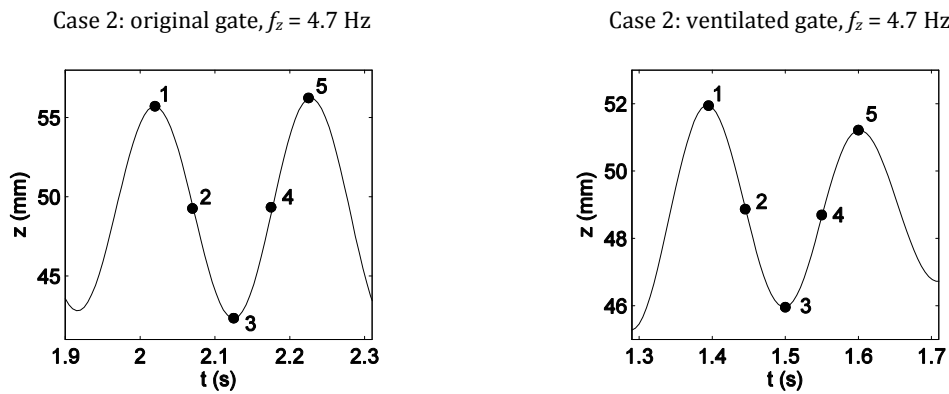


Figure 6.10. Spatial variation of hydrodynamic pressure on the gate bottom boundary for both gate types. Thick dashed lines indicate fixed gate scenario. The vertical dashed lines show the location of the ventilation slot.

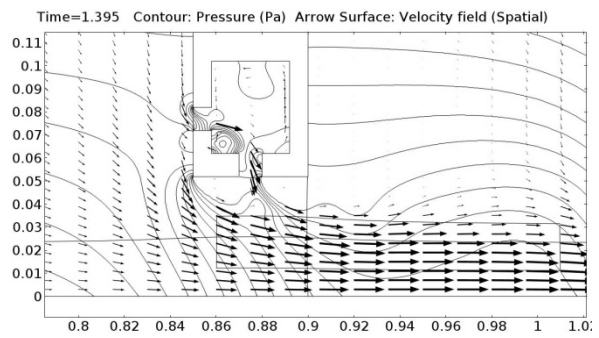
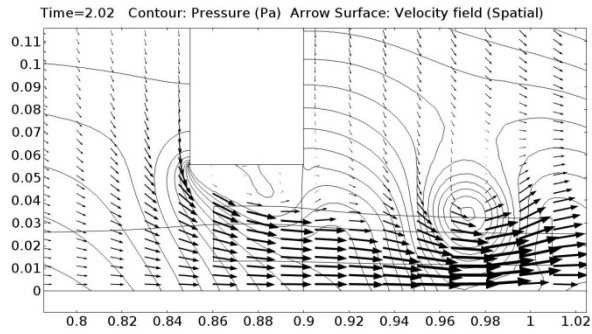
The effect of the downward jet through the hole on v -velocity (Figure 6.8) is that the outflow direction through the slot is now almost completely downward during the whole oscillation period, whereas significant upward velocities exist for the original gate. The TKE plots in Figure 6.9 show that the TKE maximum is greatly reduced. In the ventilated case, there are no large TKE levels close to the gate and maximum levels occur around $z = 0.75a$. The asymmetric shape of the TKE profile of the ventilated gate is due to the combined presence of two shear layers, resulting from flow separation from the downstream edge of the slot outlet (upper part of profile) and from the leading edge of the gate bottom (lower part of profile).

The boundary pressures in Figure 6.10 are given by the pressure parameter C_p , defined as the total pressure divided by $\rho g \Delta h$. The plots indicate that the reduced temporal fluctuation for the new gate results in positive pressures during the whole cycle, whereas the boundary pressure on the original gate is largely negative in the second part of the cycle when the gate is between lowest and midway position. The spatial pressure variations towards the trailing edge of the original gate seem to signify unstable flow fluctuations. These are virtually absent at the slotted gate, for which a smooth pressure drop is visible across the outflow from the ventilation slot.

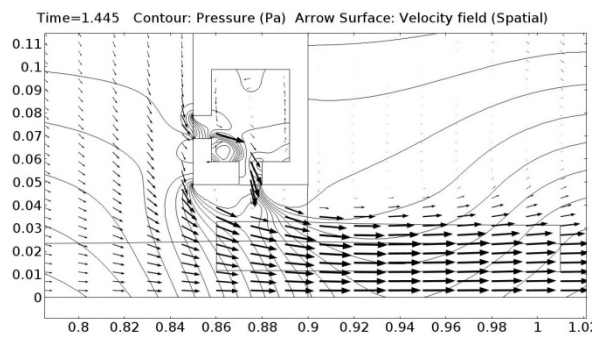
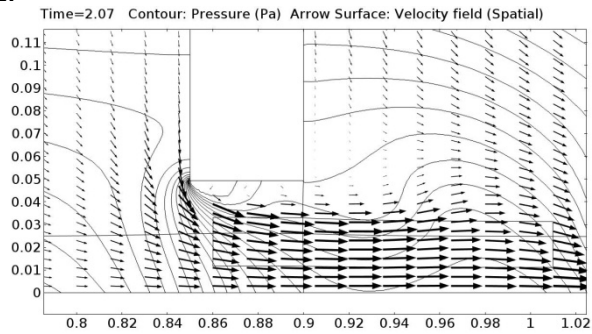
Figure 6.11 gives more simulation results of both gate types for different moments in time for one oscillation period of case 2. The flow fields of the original gate are outlined on the left and; the ventilated is on the right. Section 6.8 shows similar plots for case 1 for the original gate type.



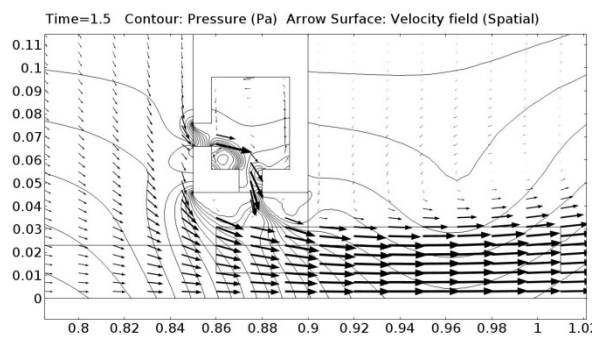
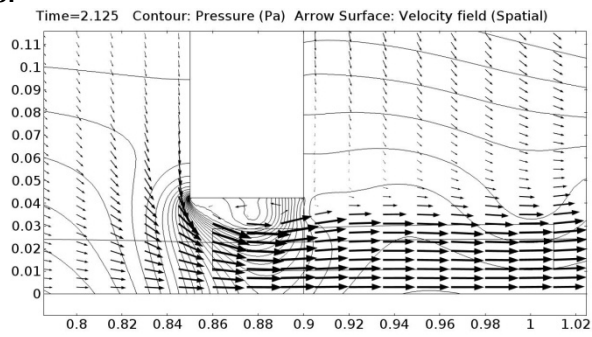
1.



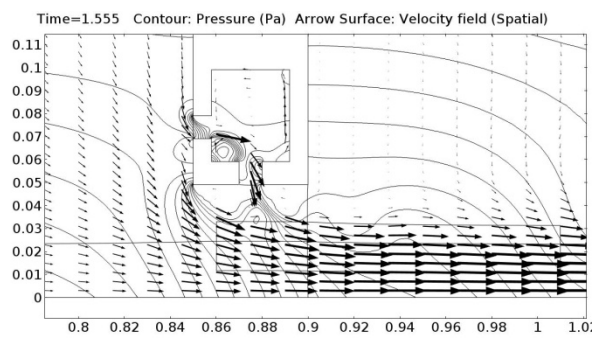
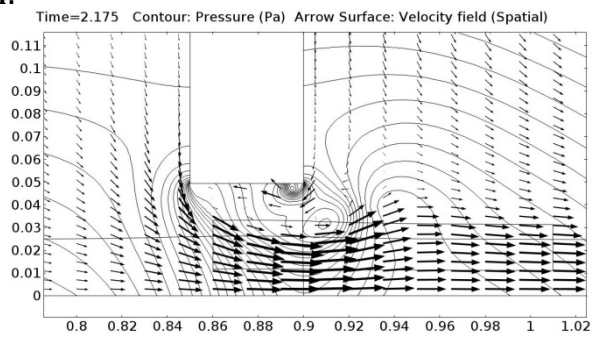
2.



3.



4.



5.

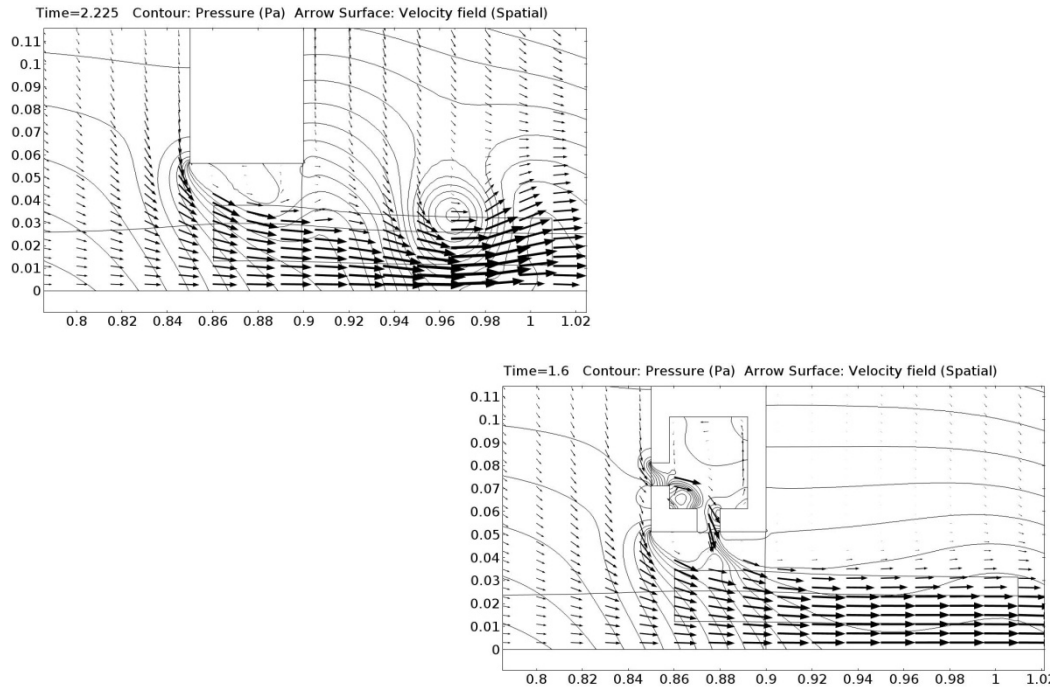


Figure 6.11. Flow velocity vectors and pressure fields for the simulated motion of both gate types for case 2 ($f = 4.7$ Hz). The plots are numbered according to the time steps of one full period as indicated in the top plots.

The plots of pressure contour lines and flow velocity vectors in Figure 6.11 serve to point out qualitative differences between the two gate types. Overall, the modified gate with ventilation slots has a flow field that is more constant in time with less vena contracta variation and less wake fluctuations. It can be seen that the flow through the slot works as an extra separated shear layer and also keeps instabilities from the wake away from the gate, see plots 3 and 4. At this time, during the first part of the upward movement, the reversion of streamwise flow velocity at the bottom boundary (which is part of a permanent recirculation zone) is strongest. Instantaneous spatial pressure gradients near the trailing edge appear for the gate without holes in plots 3 and 4. For the gate with slots this feature is not visible. This is discussed more deeply in Section 4.1 in the context of excitation. The jet through the hole persists in its downward flow during the whole oscillation period. This causes a relief in pressure build-up and prevents pressure fluctuations from the wake to enter the region under the gate. The intersections of contour pressure lines with the gate bottom present in the plots of the original gate help to illustrate the difference in pressure variations between the two gate types.

Comparing Figure 6.11 with the simulations of case 1 for the original gate in Section 6.8, it is immediately clear that case 1 has a considerably more stable flow field. The vena contracta, the large wake recirculation and the small recirculation zone under the gate hardly vary in time.

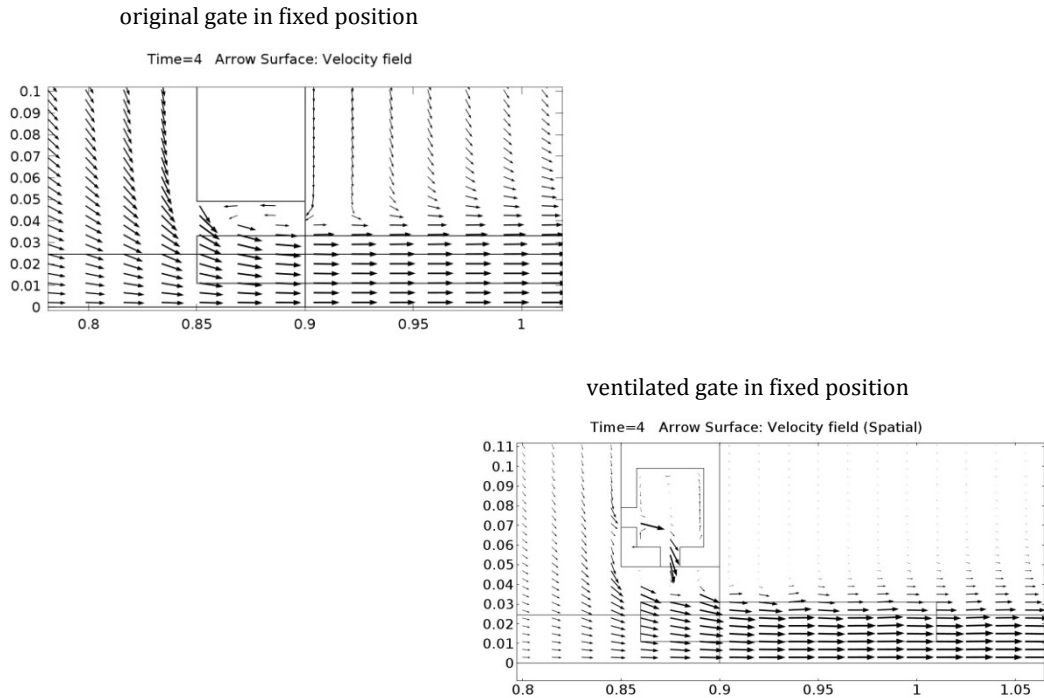


Figure 6.12. Flow velocity vectors for the situation where the gate is fixed. Boundary conditions are according to case 2. The gate position corresponds to the equilibrium position of the moving gate simulations as given in Figure 6.11.

Additional transient simulations with the gate held fixed (Figure 6.12) again show the stronger reversed flow along the gate bottom for the gate without slots. There is also evidence for flow entering the near-bottom region from downstream, similar to plot 4 of Figure 6.11. This entrainment feature is discussed in the next section. Table 6.2 gives the maximum flow velocities for the simulations. Velocities are much higher in the situation where the gate is free to move. There is little difference between the two gate types regarding maximum velocity. For the moving gate scenario the maxima were attained during the first part of the downward movement of the gate.

Table 6.2. Maximum simulated flow velocities for case 2.

	moving gate	fixed gate
original gate	3.38 m/s	2.38 m/s
ventilated gate	3.30 m/s	2.40 m/s

An additional series of numerical simulations was made with a different ventilation slot design: it lacks a hollow chamber and the ventilation slot now makes a 45 degrees angle with the gate sides. The flow field plots for conditions equivalent to case 2 are included in Section 6.9. These simulations show quite similar flow characteristics as the ventilated gate type discussed thus far. There is no wake entrainment during the vibration (plot 4 of Figure 6.14),

nor when the gate is fixed (Figure 6.15). Whether the higher u -velocity at the ventilation outflow, due to the outflow angle being tilted more in streamwise direction, is beneficial, is inconclusive from these tests. Complicating factor in comparing different gate designs is that the discharge coefficients vary and therefore other upstream velocities are required to reach the same flow conditions, and moreover that different masses give different submerged natural frequencies and hence different V_r values.

6.5 Combined discussion of physical experiment and FEM modelling

6.5.1 Vibration mechanism

As explained in the introduction, past research largely agrees on the existence and working of two excitation mechanisms for cross-flow gate vibrations: ILEV and MIE (noise excitation or Extraneously Induced Excitation (EIE) is not considered here). Based on literature, the instability-induced or vortex-excited type is the most likely mechanism for the vibrations found around $V_r \approx 2.5$, while the movement-induced type is probably the dominant mechanism for the vibrations at $V_r \approx 9.5$.

Let us consider the fluid-structure dynamics of the original gate. The separation point is fixed at the sharp leading edge – irrespective of discharge and gate position – and the boundary pressure fluctuates near the trailing edge, both in space and time. However, given the fact that the strongest vibrations in the experiment occurred for conditions similar to case 1 (viz. at $V_r \approx 2.5$), it is remarkable that the simulation of case 1 vibrations damped out. Runs with adapted settings in the neighborhood of case 1 (higher or lower gate opening, higher or lower discharge) were attempted, but did not yield different results. A transient simulation of case 1 conditions with the gate held fixed showed only small flow instabilities in the shear layer, making it impossible to determine the Strouhal number and identify small-scale vortices.

Simulation case 2 displays the main feature of movement-induced excitation (MIE) or self-excitation, because not only is a motion required to initiate the vibration process, the fluctuations in the boundary excitation force do not appear at all in the transient simulation when the gate position is fixed. The fact that the phase shift φ between excitation force and displacement is close to zero and the mean lift is only negative for a quarter of the period, implies that there is no direct evidence of galloping-type MIE excitation (Billeter and Staubli, 2000).

From the vector plots of the original gate (case 2), it is apparent that a delay exists between the motion of the gate and the oscillating shear layer. During the downward gate movement (plots 1-3 in Figure 6.11), the reduction of the vena contracta lags behind the gate displacement, which results in a minimal vertical distance between the region of separated high velocity flow and the trailing edge at $t = 2.125$ s, at the lowest gate position. The profile plot of v -velocity in Figure 6.8 shows that there is mild upward flow at $x = D$ at this part of the period ($6\pi/4$ to $7\pi/4$ or $i = 6, 7$), but it occurs away from the gate, with strongest v -velocities at $z = 0.5a-0.7a$. As the gate moves upwards through the equilibrium position (plot 4 of Figure 6.11, at $t = 2.175$ s), the vena contracta attains its minimum. This leaves a sizeable gap between separated flow and gate bottom. Clearly visible from the same plot, entrainment from the wake into the recirculation zone directly under the gate leads to high local

velocities around the trailing edge. For a short time there is a small region of relatively low pressure at the trailing edge and the reverse flow coming from the wake seems to separate from the trailing edge as it moves from right to left in Figure 6.11, plot 4. This phenomenon is reflected in the profile plots in Figure 6.7 by negative u -velocities at $0.8a < z < a$ for $i = 7, 8, 0, 1$. The highest TKE levels are found at the same part of the period, see Figure 6.9. The gate appears to receive a significant upward push from the pressure fluctuations associated with the entrainment. If this happens right at this moment of the period ($t = 2.175$ s, time step 4 in Figure 6.11), as the results suggest, then this push does positive work on the gate motion, since it is in phase with the gate velocity. The vector plot suggests that this push takes place at $x = 0.6D-0.7D$. However, the boundary pressure plot (Figure 6.10) contains small dents for $i = 7, 8, 0, 1$ around $x = 0.9D$, indicating that it might happen closer to the trailing edge. The movies of the original gate in the supplementary on-line material provide further visual support of this excitation process.

Kolkman and Vrijer (1987) reported on a mechanism based on streamwise flow inertia caused by the discharge not instantly adapting to the new gate position during low frequency vibrations at small gate openings. Because the discharge is never choked in the numerical model, this mechanism is by definition not simulated. However, the role of this mechanism cannot easily be put aside, judging from the prominent streamwise pressure irregularities in the simulations.

6.5.2 Effect of flow through the ventilated gate

Comparing the described entrainment effect of the original flat-bottom gate to the flow dynamics of the ventilated gate, as plotted in Figure 6.11, it is seen that the vena contracta does not experience the same oscillatory variation. The free shear layer and the high velocity separated flow maintain a constant, safe distance from the gate bottom. Moreover, there are no signs of wake entrainment for the ventilated gate, so that an excitation by this mechanism must be absent. The profile plots in Figures 6–10 demonstrate the lack of near-bottom pressure fluctuations capable of excitation by the virtual absence of negative u -velocities and positive v -velocities and much smaller TKE levels. The flow fields for the fixed gates (Figure 6.12) illustrate the differences between the two gate types as well: the original gate shows reverse flow near the trailing edge and a significant recirculation bubble under the gate, while the two recirculation zones under the ventilated gate (that are visible only from close inspection) are smaller in size and have negligibly small velocities.

For the MIE mechanism, the general working of the leakage flow through the ventilated gate is that it alleviates the fluctuation of the streamwise pressure and the fluctuation of the boundary pressure (thus reducing or removing negative lift). In particular, it works by preventing wake fluctuations from entering the near-gate region. The simulations were unfortunately unable to capture the effect of added slots in the case of vibration due to ILEV. It is plausible, however, that the leakage flow in this case disrupts the separated shear layer and vortices shed from the leading edge. The downward flow would consequently remove instabilities from the gate bottom and hence reduce the probability and impact of unstable reattachment.

The jet that flows out the middle of the bottom boundary not only removes local disturbances from the vicinity of the gate, as we have seen, but also has the effect of splitting

the flat bottom surface into two parts as if there were two thin gates. This is favourable since thinner profiles are less prone to vibrations, or at least reduce the risky gate opening region. An alternative explanation of the response reduction could be found in the fact that the presence of the slot simply decreases the surface area for the lift pressure to work on. However, simulations of a closed rectangular gate with a bottom surface area equivalent to that of the gate with a hole showed that the diminished dynamic force amplitude cannot be explained by the smaller area. The different response must therefore be caused by the leakage flow.

The location of the outflow openings and the angle at which the jets flow (relative to the gate's bottom surface and the mean flow) are undoubtedly important design parameters. Another factor is the widthwise distribution of the slots in the design, that is, the distance between consecutive openings. A jet originating from flow through a small circular opening into a wide domain expands in all three dimensions, this is related to entrainment of surrounding fluid of relatively low velocities, an inherently turbulent process. The situation of flow through horizontal slots in the present study is different from the canonical jet, since the openings are elongated in one direction and the outflow domain has strong velocity gradients. The spaces between the slots, that were necessary in the present design to preserve structural rigidity, influence the outflows from the gate bottom slots and the three-dimensional aspect of the flow. So, although the slot configuration in this study is symmetric around the middle of the gate, three-dimensional flow phenomena may play a non-negligible role. The impact of this on gate stability and the effectiveness of the leakage flow can only be clarified through additional physical and numerical modelling.

6.5.3 Implementation in prototype gates

In principle, there is no reason why the ventilated gate design would not be applicable to an actual gate. The gate would function as a conventional gate most of the time, with an added leak flow discharge through the ventilation slots. Perhaps the most critical issue is the gate's behaviour at very small gate openings, directly prior to full closure. In closed position, the leakage flow through the slots must be zero. This requires good seals that at the same time should not deteriorate the vibration properties of the gate's bottom geometry. The idea to add a movable element (gate or valve) to control the inflow through the upstream inflow slots seems interesting, but of course might engage itself in flow-induced vibrations. Another point of attention would be to prevent the accumulation of sediment and trash inside the ventilation holes.

6.5.4 Evaluation of numerical modelling

The rigid-lid approach makes it impossible for the model to capture the effect of wave radiation. This is a form of hydraulic damping that involves vibration energy to be transformed irreversibly into free-surface waves. Not modelling this is not a severe omission, see also section 3.2. In the experiment wave radiation was only observed once at the upstream water surface in the low stiffness vibration region. Another free-surface effect that is completely neglected by using the rigid lid approximation is the coupling of flow-induced undulations of the downstream surface with the gate oscillation at increasing Froude number (see Naudascher and Rockwell, 1994). However, these undulations only occur at much lower submergence levels than investigated in this study. A consequence of the fixed free surface boundary in connection with the constant discharge is furthermore

that global pressure oscillations are exaggerated. A lowering of the gate results in an immediate pressure increase in the upstream region, for instance. It is not easily found to what extent this affects the emergence of gate instabilities in the simulations; there is presumably a link with the representation of the MIE vibrations. The complication of this numerical modelling aspect lies in the fact that methods that do simulate the free surface (such as Volume Of Fluid or Phase Field) are usually not suitable for including both moving objects and turbulent flow, or they are computationally impractically expensive.

In physical experiments, comparisons of measured gate displacement and excitation force cannot always distinguish between added mass and rigidity since both coefficients are part of terms in-phase with the displacement (e.g. Kolkman 1984). Similarly, in a numerical study it is not sufficiently clear whether a deviating response frequency should be attributed to artificial mass or rigidity effects. Either way, the distorting influence of artificial added coefficients must be elucidated before the full working of all physical mechanisms can be uncovered by numerical modelling.

Artificial damping or numerical diffusion can be traced back to the use of an implicit time scheme and 'consistent stabilisers' (COMSOL 2013). The effect of this is inherent to the followed numerical approach; without it the simulation of the flow fails. Naturally, too much artificial damping of turbulent flow results in vibrations not being induced in the simulations where they do occur in real life. In particular, negative damping plays a key role in self-excited vibrations – if negative damping is neutralised by artificial factors, MIE-type vibrations will be inaccurately represented. As mentioned in Section 4.1, another limitation of the numerical model is the constant discharge that in real life fluctuates as a result of gate displacements (most prominently for low frequency oscillations at small gate openings).

Finally, the obvious limitation of the RANS approach with a turbulence model is that not all turbulence scales are simulated. The fact that vortex shedding and velocity and pressure fluctuations at small-length scales connected to the shear layer are parametrised too coarsely could be the reason why the (presumably ILEV-dominated) vibrations of case 1 were not reproduced. Applying a different turbulence model is unlikely to improve this; Large Eddy Simulation (LES) could be the only way forward.

6.6 Combined conclusions of physical experiment and FEM modelling

The goal of this the this chapter and the previous one was to experimentally and numerically test a new hydraulic gate design for reducing flow-induced cross-flow vibrations. The addition of ventilation slots to a rectangular flat-bottom gate allowed a controlled leakage flow through the bottom of the gate, which produced a less severe vibration response compared to an unaltered reference gate.

The experimental data set fully covers the transitions between conditions with and without significant flow-induced vibrations in the reduced velocity region $2 < Vr < 3.5$. Two distinct vibration regimes are recognized with maximum response force amplitudes at $Vr = 2.54$ and $Vr = 10.16$ for gate openings $a/D = 0.48$ and $a/D = 0.86$, respectively. The results show that the gate with perforated bottom profile significantly reduces cross-flow vibrations in the region $2 < Vr < 3.5$. Although not exhaustively covered, the measurements give reason to

believe that the same holds for the higher region at $Vr > 8.5$. It was found that damping appeared to be higher for high hydraulic heads, but this did not affect the comparison between the two gate types.

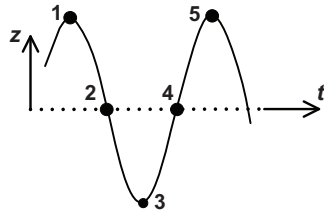
The obtained data set was used to evaluate and improve the performance of a numerical model. Time-dependent FEM simulations on a moving grid were performed to solve the RANS equations for the flow and the gate displacement of the mass-spring system. An initial model validation step for the added mass in still water showed reasonable estimates compared to the measurements and reproduced the wall proximity effect. Subsequently, as a form of calibration, the sensitivity of the response frequency in flowing water to variation of the mass factor was used to select an appropriate solid density and spring stiffness while keeping the natural frequency in air equal to experimental values. Then, two cases of strong vibrations were simulated from the low and high Vr regions. For the high Vr case with response frequency 4.7 Hz, vibrations with growing amplitude were reproduced for the rectangular gate while the modified gate with a hole showed decreasing amplitudes in the same conditions. This matches results from the physical experiment.

Even though the numerical model does not capture all features relevant for a complete representation of the excitation mechanisms, the results nevertheless give valuable information about the working of the new gate design. The downward jets through the slots remove flow instabilities from the bottom boundary and smoothens local pressure gradients. In particular, the simulations show that for the standard rectangular gate, entrainment from the wake into the zone directly under the gate leads to a transfer of momentum from the flow to the gate. This movement-induced excitation is absent in the gate with slots, because the leakage flow prevents this entrainment.

6.7 Summary

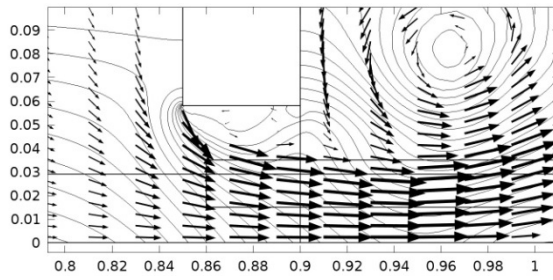
Two-dimensional numerical simulations were performed with the Finite Element Method to assess local velocities and pressures for both gate types. A moving mesh covering both solid and fluid domain allowed free gate movement and two-way fluid-structure interactions. Modelling assumptions and observed numerical effects are discussed and quantified. The simulated added mass in still water is shown to be close to experimental values. The spring stiffness and mass factor were varied to achieve similar response frequencies at the same dry natural frequencies as in the experiment. Although it was not possible to reproduce the vibrations dominated by impinging leading edge vortices (ILEV) at relatively low Vr , the simulations at high Vr showed strong vibrations with movement-induced excitation (MIE). For the latter case, the simulated response reduction of the ventilated gate agrees with the experimental results. The numerical modelling results suggest that the leakage flow diminishes pressure fluctuations close to the trailing edge associated with entrainment from the wake into the recirculation zone directly under the gate that most likely cause the growing oscillations of the ordinary rectangular gate.

6.8 Additional simulations: flow velocity and pressure of case 1



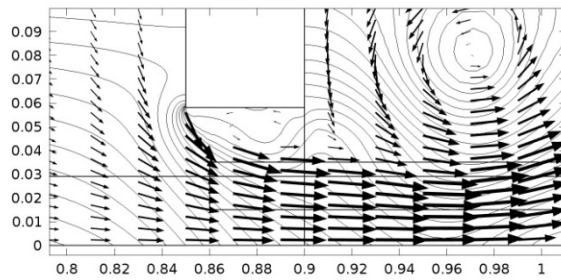
1.

Time=0.595 Contour: Pressure (Pa) Arrow Surface: Velocity field (Spatial)



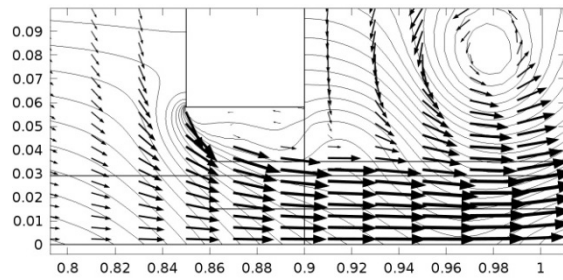
2.

Time=0.62 Contour: Pressure (Pa) Arrow Surface: Velocity field (Spatial)



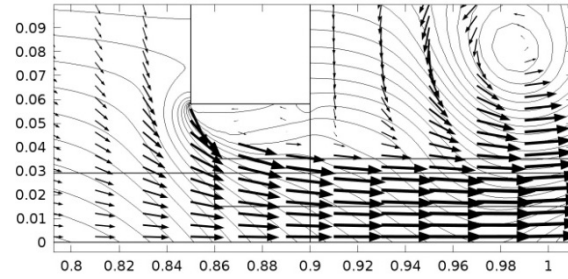
3.

Time=0.645 Contour: Pressure (Pa) Arrow Surface: Velocity field (Spatial)



4.

Time=0.67 Contour: Pressure (Pa) Arrow Surface: Velocity field (Spatial)



5.

Time=0.695 Contour: Pressure (Pa) Arrow Surface: Velocity field (Spatial)

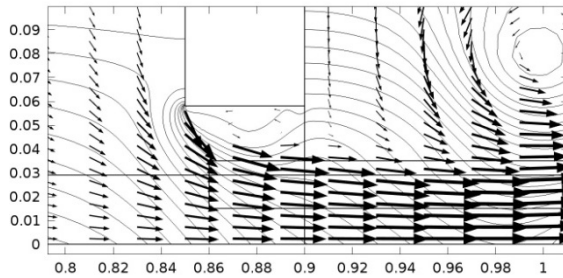
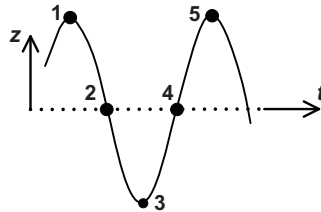


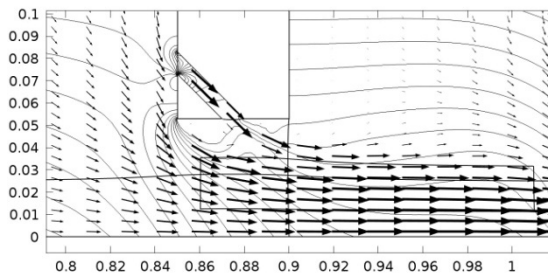
Figure 6.13. Simulated flow fields of one cycle for case 1, original gate, $f_z = 10.1$ Hz.

6.9 Additional simulations: an alternative ventilation design



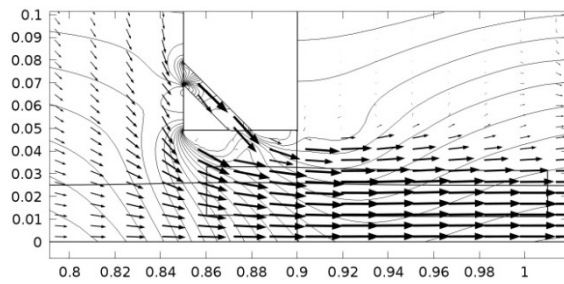
1.

Time=1.215 Contour: Pressure (Pa) Arrow Surface: Velocity field (Spatial)



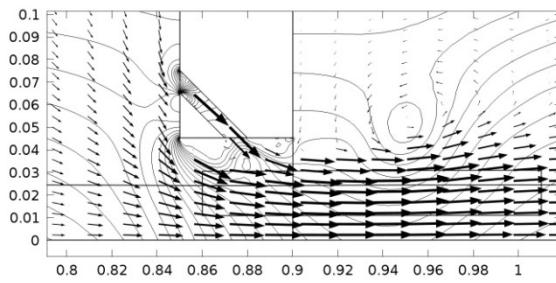
2.

Time=1.27 Contour: Pressure (Pa) Arrow Surface: Velocity field (Spatial)



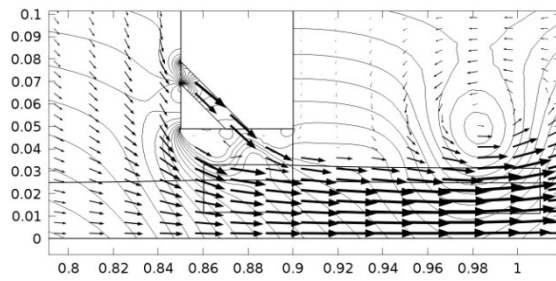
3.

Time=1.325 Contour: Pressure (Pa) Arrow Surface: Velocity field (Spatial)



4.

Time=1.375 Contour: Pressure (Pa) Arrow Surface: Velocity field (Spatial)



5.

Time=1.425 Contour: Pressure (Pa) Arrow Surface: Velocity field (Spatial)

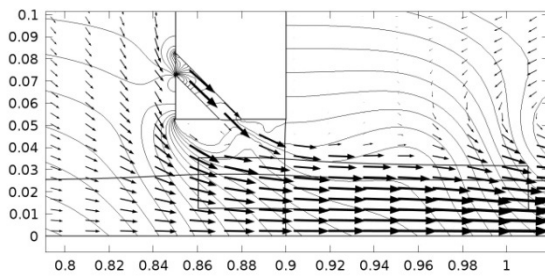


Figure 6.14. Simulated flow field of alternative slot design for case 2, $f_z = 4.7$ Hz.

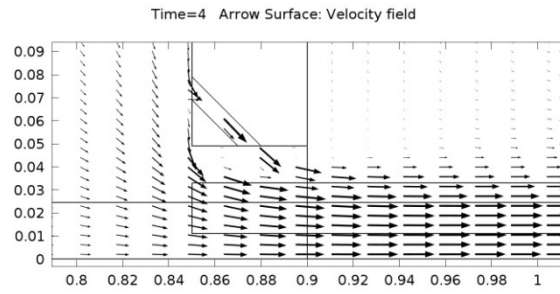


Figure 6.15. Simulated flow field of alternative slot design with gate in fixed position.

The maximum global flow velocity magnitude of this gate geometry for case 2 is 3.22 m/s and 2.36 m/s for the fixed gate case.